Supporting Information

Scalable microfluidic fabrication of vertically aligned two-dimensional nanosheets for superior thermal management

Kai Yang[a], Xiaoran Yang[a], Zexin Liu[b], Rong Zhang[a], Yue Yue[b], Fanfan Wang[a], Kangyong Li[a], Xiaojie Shi[c], Jun Yuan[e], Ningyu Liu[e], Zhiqiang Wang[c]*, Gongkai Wang[d]*, Guoqing Xin[a]*

[a]*Wuhan National High Magnetic Field Center and School of Materials Science & Engineering, Huazhong University of Science and Technology, Wuhan 430074, China*

[b]*School of Chemistry and Chemical Engineering, Huazhong University of Science and Technology, Wuhan 430074, China*

[c]*School of Electrical and Electronic Engineering, Huazhong University of Science and Technology, Wuhan 430074, China*

[d]*School of Material Science and Engineering, Research Institute for Energy Equipment Materials, Hebei University of Technology, Tianjin, 300130, China*

[e]*Dept of Integrated Power Systems and Device Technology, Hubei Jiufengshan Laboratory, Wuhan 430206, China*

Corresponding authors. E-mail: zhiqiangwang@hust.edu.cn (Z.W.), wang.gongkai@hebut.edu.cn (G.W.), guoqingxin@hust.edu.cn (G.X.)

List of content

1、**Supplementary Methods**

2、**Supplementary data**

Figure S1. Vertically aligned 2D MoS_2 and boron nitride (BN) nanosheet films prepared by MSAP.

Figure S2. Alignment and orientation of GO nanosheets inside the microfluidic device.

Figure S3. Calculated shear stress on the longitudinal section of different wide microchannels.

Figure S4. Rotation of GO nanosheets in expansion zone by extensional stress.

Figure S5. The geometry of the longitudinal section of the microchannel array mold with a microchannel width of 200 μm in CFD simulation.

Table S1. Material properties used in the simulation.

Figure S6. Rheology of GO dispersion.

Figure S7. The average lateral size of GO nanosheets.

Figure S8. Improvement of crystallinity, removal of functional groups, lattice defects/ vacancies recovery of VANF-G by 2950 ℃ thermal annealing.

Figure S9. Confirmation of metal-level thermal conductivity of TIMs.

Figure S10. Calculation of the thermal conductivity for graphene sheets filler, K_p, and measurement of the thickness for graphene sheets, h.

Figure S11. Compressive stress-strain curve of TIMs and PDMS.

Figure S12. The test system configuration for the collection of IR images of the MOSFET device.

Figure S13. Cross sectional SEM images of TIM composite before and after temperature cycling test.

Table S2. Comparison of through plane thermal conductivities of our TIMs composites with reported graphene/polymer composites.

Movie S1. This movie shows the continuous and scalable fabrication of vertically aligned GO nanosheets film by microfluidics-enabled sheets aligning process.

Movie S2. This movie shows the real-time polarized microscopy observation of GO dispersion outflowing from microchannel arrays with different width of 30 μm, 100 μm and 200 μm respectively.

3、Supplementary References

Supplementary Methods

In situ SAXS measurement: In order to get high X-ray transmission for in situ SAXS measurements, polyimide rectangular microchannels with 100 μm in width have been applied. To collect SAXS signal, microchannel was placed horizontally and GO dispersion was pumping through the microchannel. SAXS measurements were carried out on a Bruker Nanostar-U instrument with a rotating anode X-ray source, operated at 50 kV and 24 mA. The SAXS detector was a multi-wire proportional counter (Bruker Hi-Star) with 1,024×1,024 pixels and a beryllium front window 11.5 cm across. The SAXS detector was placed 105 cm from the sample, allowing measurement of scattering angles from 0.2 to 2.8° (2θ).

Computational fluid dynamics simulations: The non-Newtonian flow behavior of the

GO dispersion was characterized by a shear rate-dependent viscosity. The shear rate–viscosity data from rheology measurements were described by the Herschel–Bulkley model, $\tau = \tau_y + K\dot{\gamma}^n$ (plotted in Figure S5) and applied to fluid dynamics simulations.

Equation of motion for momentum conservation of GO fluid are described by the Navier–Stokes equation with the shear rate-dependent viscosity:

$$\nabla \cdot v = 0 \quad \#(1)$$

$$\rho\partial_t v + \rho(v \cdot \nabla)v = \nabla \cdot \left[-pI + \eta\left(\nabla v + \nabla v^T\right)\right] \#(2)$$

with constant density of the fluid ρ and unity matrix I. The equation was solved with COMSOL Multiphysics v5.6 software. First, the microchannel geometry designed by SolidWorks was imported into COMSOL, and the finite elements were generated based on the geometry. Figure S5 shows the geometry of 2D longitudinal section of the microchannel array mold. As shown in Figure S6, the Herschel–Bulkley model was used to obtain the relevant parameters, including yield stress (τ_y), Fluid consistency coefficient (K), and power-law exponent (n). Boundary conditions were given to finite elements and corresponding experimental parameters were added to match the experimental conditions (Table S1). Finally, velocity field distribution, elongational rate, extensional rate and shear stress were obtained from the simulation.

The measurements of VANF-G's orientation order σ with angle-resolved Polarized Raman Spectroscopy: The excitation polarized laser with a wavelength of 532 nm was focused onto the sample through an objective lens (100x, NA 0.9). The polarization direction was controlled with a half-wave plate, and the half wave plate is inserted into the common optical path of the incident laser and the scattered Raman

signal to change their polarization direction at the same time. A polarized analyzer is applied to detect the scattered Raman signal intensity and set in direction perpendicular to the incident laser. By optimizing integration times and exposure time, Raman spectra with sufficient signal-to-noise ratio can be obtained. The polarized Raman intensity depends on the polarization angle, φ, of the incident laser beam, and the angular dependence of the Raman peak intensity, $I_{tot}(\varphi)$, is fitted with the following function:[1]

$$I_{tot}(\varphi) = I_0 \cdot \left\{ \frac{8}{15} + \langle P_2(\cos\theta) \rangle \left(-\frac{16}{21} + \frac{8}{7}\cos^2\varphi \right) + \langle P_4(\cos\theta) \rangle \left(\frac{8}{35} - \frac{8}{7}\cos^2\varphi + \cos^4\varphi \right) \right\} \#\#(3)$$

where the constant I_0 is the amplitude, $\langle P_2(\cos\theta) \rangle$ and $\langle P_4(\cos\theta) \rangle$ are the second- and forth-order orientation factors, respectively. $\langle P_2(\cos\theta) \rangle = (3 < \cos^2\theta > - 1)/2$ is commonly known as Herman's orientation order, σ, which is equal to 1 for perfect alignment and 0 for complete random orientations. Angular dependent G band has been used to measure the orientation order. The Raman signal intensity of all samples is measured 5 times repeatedly and the corresponding σ expressed as mean $\pm$ SD (standard deviation).
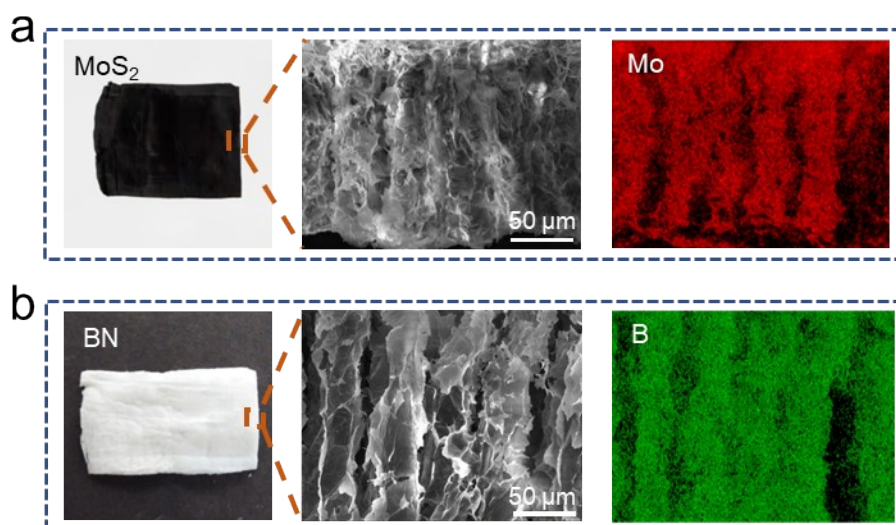
Supplementary Figures

Figure S1. Vertically aligned 2D MoS_2 and boron nitride (BN) nanosheet films prepared by MSAP. (a, b) Macro samples, cross-sectional SEM image and elemental mapping by energy dispersive spectroscopy (EDS) of (a) MoS_2 and (b) BN, respectively. The 2D MoS_2 (semiconductor) and BN (insulator) liquid crystal (LC) dispersion was synthesized to prepare samples.[2, 3] The vertical aligned nanosheets demonstrating that MSAP technique can be extended to other 2D materials.
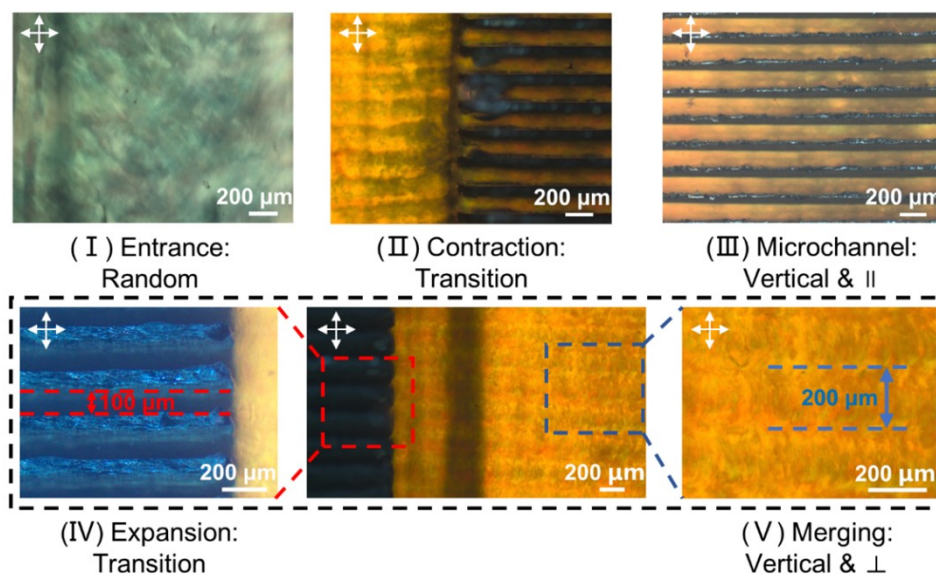
Figure S2. Alignment and orientation of GO nanosheets inside the microfluidic device. Polarized optical microscopy (POM) images showing nematic texture of GO LC in microfluidic device and indicating the alignment and orientation of GO nanosheets at different zones: (I) entrance zone, (II) contraction zone, (III) microchannel zone, (IV) expansion zone, and (V) merging zone. The microchannels width are 100 μm. The nematic texture of different regions is consistent with the 30 μm wide microchannel.
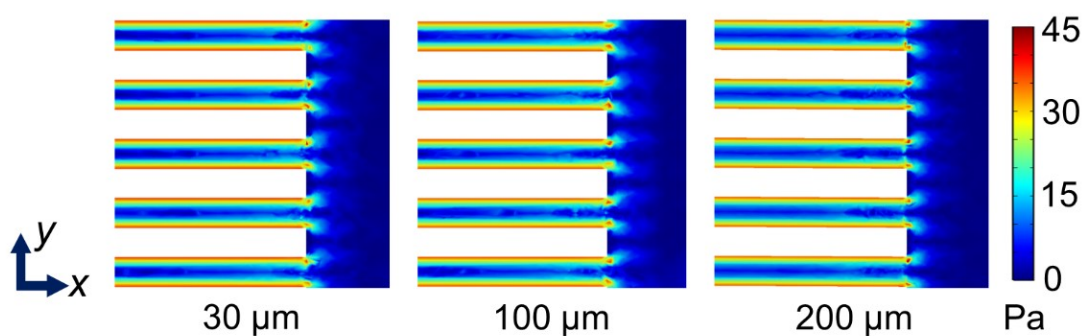

Figure S3. Calculated shear stress on the longitudinal section of the 30 μm, 100 μm and 200 μm wide microchannels, respectively. The mean flow velocities of GO dispersion are kept at 1mm/s, same for all microchannel devices. The wall shear stresses generated by all microchannel devices are nearly equal.
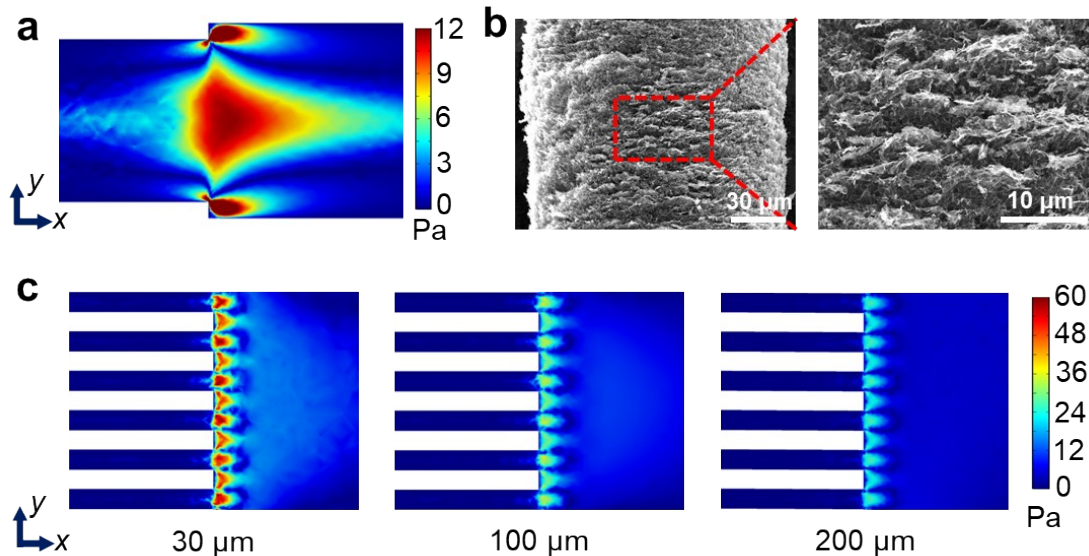
Figure S4. Rotation of GO nanosheets in expansion zone by extensional stress. (a) Calculated extensional stress on the longitudinal section of the channel, in which GO dispersion flows from a 100-μm-thick tube to a 120-μm-thick tube. (b) Microstructure of freeze-dried GO rod spun by expansion tube. The enlarged view shows vertically aligned 2D sheets, indicating that GO nanosheets can be fully rotated by low extensional stress of ~4 Pa. (c) Calculated extension stress on the longitudinal section of the 30 μm, 100 μm and 200 μm wide microchannels, respectively. The mean flow velocities of GO dispersion are 1 mm/s for all microchannel devices. The generated extension stresses in all microchannels are high enough to rotate GO nanosheets.
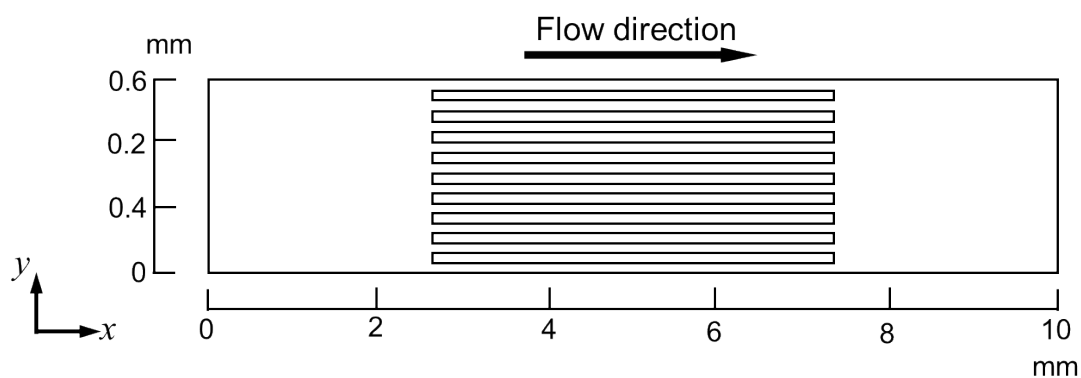
Figure S5. The geometry of the longitudinal section of the microchannel array mold with a microchannel width of 200 μm in CFD simulation.
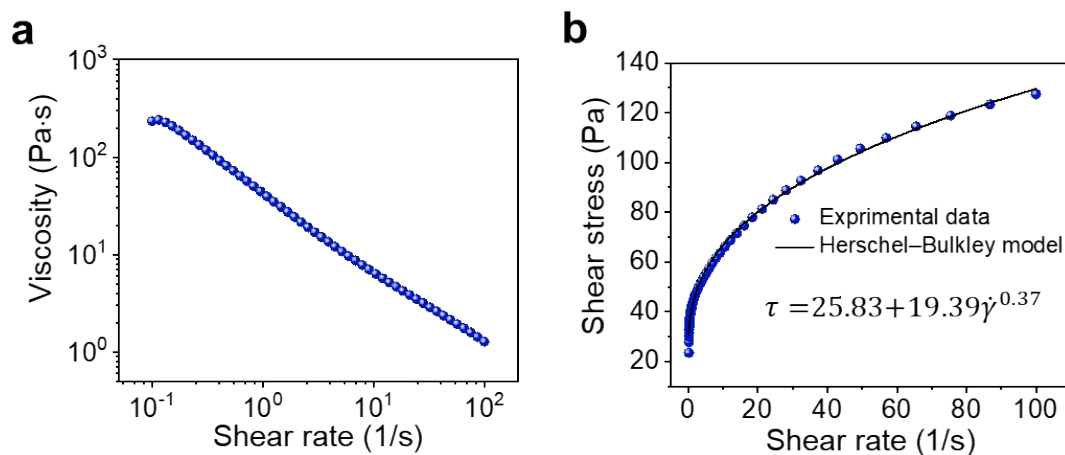

Figure S6. Rheology of GO dispersion. (a) The plot of viscosity as a function of shear rate indicates that GO suspension is a shear thinning non-Newtonian fluid, the viscosity decreases with increasing shear rates. (b) The plot of shear stress as a function of shear rate and the fitting curve by the Herschel–Bulkley model, $\tau = \tau_y + K\dot{\gamma}^n$. The yield stress τ_y is 25.83 Pa.

Table S1 Material properties used in the simulation

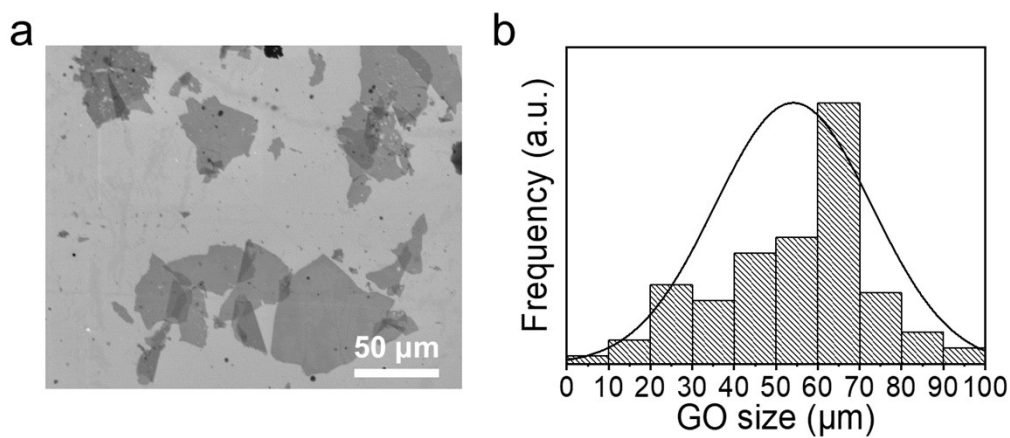| CFD Parameters	Non-Newtonian
Inlet boundary condition: flow rate ml/min	0.036
Outlet boundary condition: pressure, Pa	0
Flow speed, mm/s	1
Fluid consistency coefficient, Pa·s	19.39
Yield stress, Pa	25.83
Power-law exponent	0.37
Density, Kg/m³	1050

Figure S7. The average lateral size of GO nanosheets. (a, b) SEM image of GO nanosheets (a) and corresponding size distribution (b). The average lateral size of GO nanosheets is 54 μm.
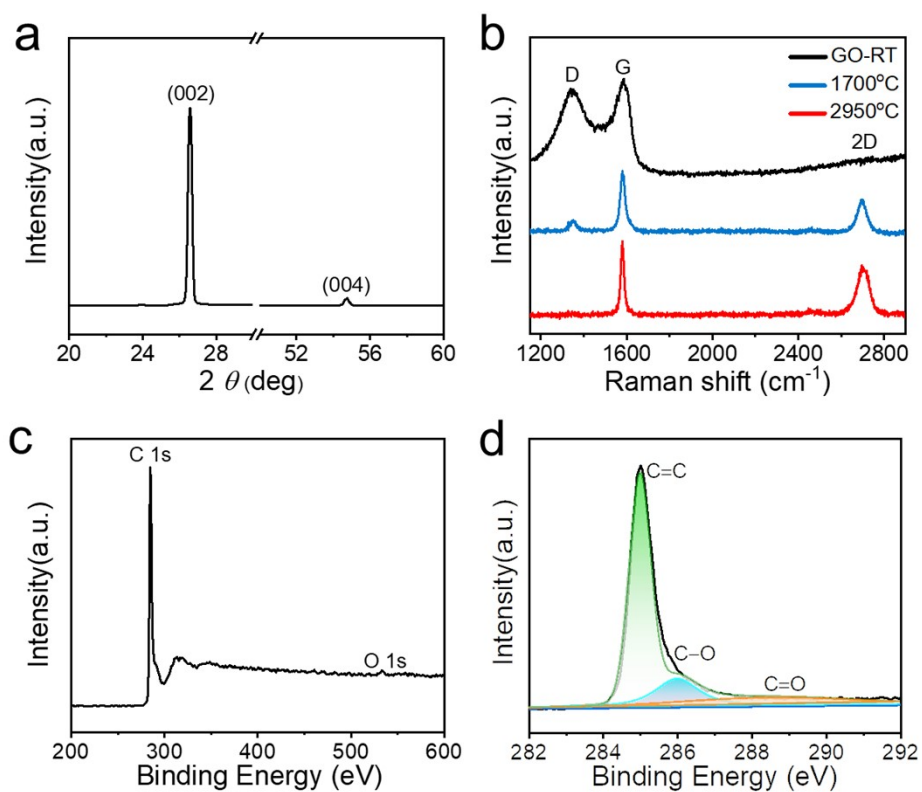
Figure S8. Improvement of crystallinity, removal of functional groups, lattice defects/vacancies recovery of VANF-G by 2950 °C thermal annealing. (a) XRD pattern. (b) Raman spectra of GO VANF and VANF-G annealed at different temperatures. (c, d) XPS spectrum (c) and deconvoluted C1s peak spectra (d).

In Figure S8, the control of defects and functional groups and improvement of crystallinity of VANF-G are confirmed by systematic structural characterization. Upon thermal treatment, the XRD pattern (**Figure S8a**) shows a strong peak at 26.56°, approaching the characteristic peak (26.7°, d-spacing ≈ 3.33 Å) of pure graphite, indicating a high degree of graphitization of VANF-G achieved.[4] On Raman spectrum of the GO VANF, the D-band near 1350 cm^{-1} evolved from lattice defects/vacancies created by the attachment of oxygen groups on the carbon basal plane. Upon thermal annealing at 1700 °C, the D band is depressed with G band becoming much narrower.

The disappearance of D band and recovery of 2D band after 2950 °C thermal annealing indicate the removal of defects and recovery of crystallinity of graphene sheets (**Figure S8b**). On XPS spectrum, the absence of O1s peak (**Figure S8c**), removal of oxygen functional groups and dominant C=C sp^2 hybridization (**Figure S8d**) upon thermal annealing indicate that oxygen functional groups and lattice defects on graphene sheet have been removed upon thermal annealing.[5]
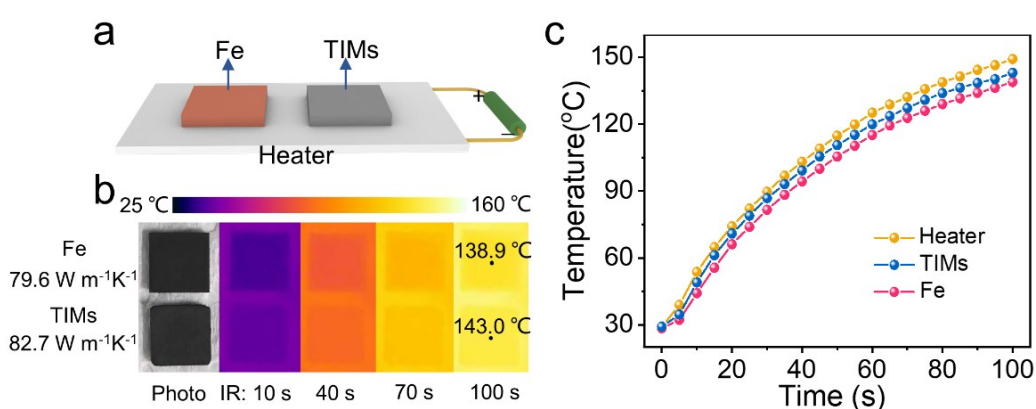

Figure S9. Confirmation of metal-level thermal conductivity of TIMs. (a) Test system configuration for demonstrating the through-plane heat transfer capacity. (b, c) Surface IR images (b) and corresponding temperature evolution of the TIMs and pure Fe versus heating time (c). The temperature of the TIMs increases relatively faster than that of pure Fe and always shows a slightly higher value (e.g., $\Delta T = 6.2$ °C at 100 s), demonstrating the higher through-plane thermal conductivity of the TIMs compared to that of pure Fe.
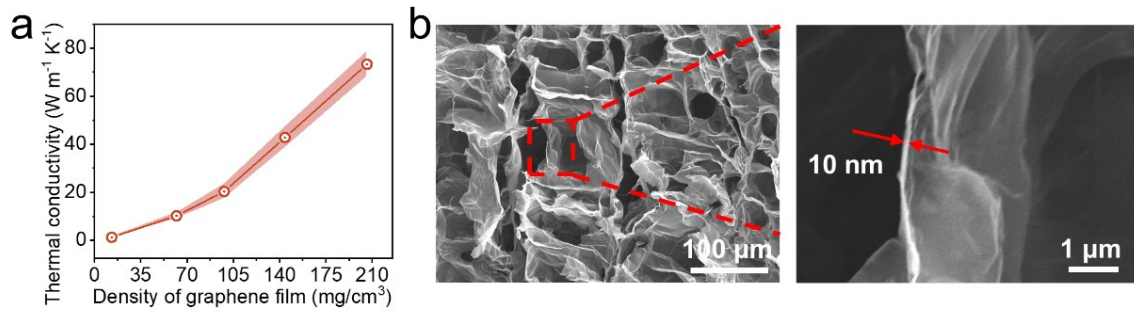
Figure S10. Calculation of the thermal conductivity for graphene sheets filler, K_p, and measurement of the thickness for graphene sheets, h. (a) Thermal conductivities of VANF-G as a function of density. The thermal conductivity of VANF-G has been measured as 73.3 W m^{-1}K^{-1} at density of 0.206 g/cm^3. According to the density of pure graphite (2.2 g/cm^3), the thermal conductivity of graphene sheets filler, K_p, has been calculated as 780 W m^{-1}K^{-1}. (b) SEM images of VANF-G after removal of the top skin layer. Enlarged SEM images show that the graphene sheets thickness is 10 nm approximately.
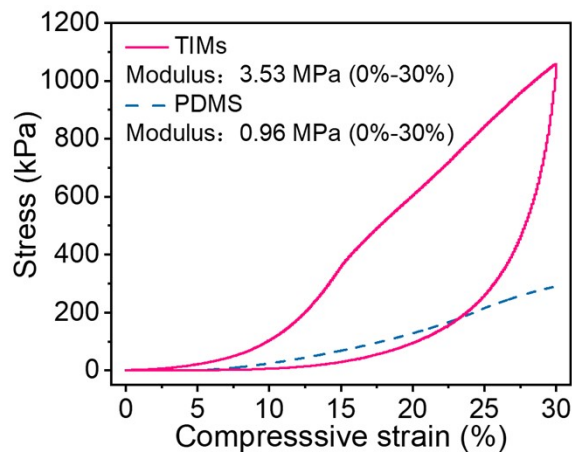

Figure S11. Compressive stress-strain curve of TIMs and PDMS.

In the actual application of thermal interface materials (TIMs), a vertical deformation is needed under a moderate packaging pressure (~1 MPa) to ensure a good

contact between the applied TIM and heater/heat sink.[6] As shown in **Figure S11**, under a normal strain range from 0% to 30%, the compressive stress of TIMs exhibits a change from 0 to 1.02 MPa, which are in good agreement with the mechanical property requirements of commercial TIMs and normal packaging pressure. The compressive modulus of the sample was obtained by calculating the average value of the tangent modulus ($E = d\delta/d\varepsilon$) in the range of 0–30% strain, where δ is the compressive stress and ε is the corresponding strain. The calculated results give a lower compressive modulus of TIMs (3.53 MPa) compared to other reported silicone-based composites (3.8−10 MPa), indicating an adequate deformation capacity for TIMs to yield a satisfactory gap-filling.[7-11]
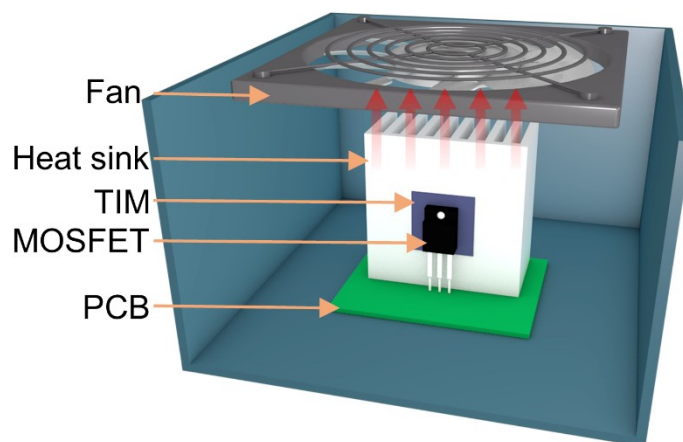

Figure S12. The test system configuration for the collection of IR images of the MOSFET device. TIM between the MOSFET and the heat sink are the key medium to transfer the heat generated by the MOSFET to the heat sink and finally the heat is dissipated out by the fan above the heat sink.
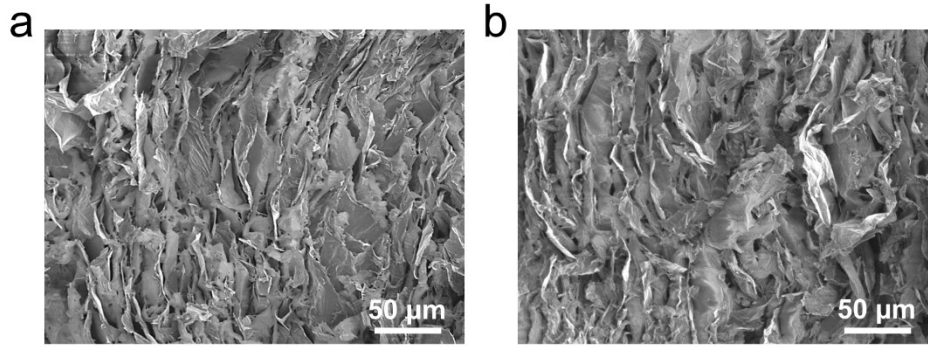
Figure S13. (a, b) Cross sectional SEM images of TIM composite before (a) and after (b) temperature cycling test. TIM's microstructure shows that graphene sheets are still in good contact with PDMS matrix after test, without any TIM dry-out seen.

Table S2. Comparison of through plane thermal conductivities of our TIMs composites with reported graphene/polymer composites.[12-24]

Filler	Matrix	Thermal Conductivity (W m^{-1} K^{-1})	Graphene Content (vol%)	TCE (%)	Ref.
VANF-G	PDMS	82.7	~11.8	45844	This work
Dual-assembled graphene framework	PDMS	60.2	13.3	33160	[12]
Covalently bonded graphene nanowalls	PDMS	20.4	~2.8	11233	[13]
Lamellar-structured graphene aerogels	Epoxy	20	2.3	9913	[14]
Graphene framework	Epoxy	5.4	~2.7	2650	[15]
Graphene-multilayer	Epoxy	5.1	~10	2300	[16]
Graphene nanoflake	PVDF	10	~25	7592	[17]
3D graphene aerogel	Wax	8.87	1.31	1858	[18]
Multilayer graphene	Epoxy	1.5	2.8	650	[19]
Vertically Aligned Graphene Networks	Epoxy	2.13	0.92	1332	[20]
Aligned graphene nanosheets foam	Rubber	10.66	6.2	8100	[21]
Binary-filler with graphene and copper	Epoxy	13.5	20	6650	[22]
Vertically aligned graphene foams	Epoxy	35.5	19	19622	[23]
Vertically aligned graphene aerogels	Epoxy	6.57	0.75	3550	[24]

Supplementary References

1. Z. Li, R. J. Young, I. A. Kinloch, N. R. Wilson, A. J. Marsden and A. P. A. Raju, *Carbon*, 2015, **88**, 215-224.

2. R. Jalili, S. Aminorroaya-Yamini, T. M. Benedetti, S. H. Aboutalebi, Y. Chao,

G. G. Wallace and D. L. Officer, *Nanoscale*, 2016, **8**, 16862-16867.

3. W. Lei, V. N. Mochalin, D. Liu, S. Qin, Y. Gogotsi and Y. Chen, *Nat. Commun.*, 2015, **6**, 8849.

4. G. Xin, T. Yao, H. Sun, S. M. Scott, D. Shao, G. Wang and J. Lian, *Science*, 2015, **349**, 1083-1087.

5. G. Xin, W. Zhu, Y. Deng, J. Cheng, L. T. Zhang, A. J. Chung, S. De and J. Lian, *Nat. Nanotechnol.*, 2019, **14**, 168-175.

6. J. Hansson, T. M. J. Nilsson, L. Ye and J. Liu, *Int. Mater. Rev.*, 2017, **63**, 22-45.

7. W. Zhang, Q. Q. Kong, Z. Tao, J. Wei, L. Xie, X. Cui and C. M. Chen, *Adv. Mater. Interfaces*, 2019, **6**, 1900147.

8. S. Bhanushali, P. C. Ghosh, G. P. Simon and W. Cheng, *Adv. Mater. Interfaces*, 2017, **4**, 1700387.

9. Q. Zhang, X. Xu, H. Li, G. Xiong, H. Hu and T. S. Fisher, *Carbon*, 2015, **93**, 659-670.

10. S. H. Jeong, S. Chen, J. Huo, E. K. Gamstedt, J. Liu, S. L. Zhang, Z. B. Zhang, K. Hjort and Z. Wu, *Sci. Rep.*, 2015, **5**, 18257.

11. K. Uetani, S. Ata, S. Tomonoh, T. Yamada, M. Yumura and K. Hata, *Adv. Mater.*, 2014, **26**, 5857-5862.

12. W. Dai, L. Lv, T. Ma, X. Wang, J. Ying, Q. Yan, X. Tan, J. Gao, C. Xue, J. Yu, Y. Yao, Q. Wei, R. Sun, Y. Wang, T. H. Liu, T. Chen, R. Xiang, N. Jiang, Q. Xue, C. P. Wong, S. Maruyama and C. T. Lin, *Adv. Sci.*, 2021, **8**, 2003734.

13. Q. Yan, F. E. Alam, J. Gao, W. Dai, X. Tan, L. Lv, J. Wang, H. Zhang, D. Chen, K. Nishimura, L. Wang, J. Yu, J. Lu, R. Sun, R. Xiang, S. Maruyama, H. Zhang, S. Wu, N. Jiang and C. T. Lin, *Adv. Funct. Mater.*, 2021, **31**, 2104062.

14. P. Liu, X. Li, P. Min, X. Chang, C. Shu, Y. Ding and Z. Z. Yu, *Nano-micro Lett.*, 2020, **13**, 22.

15. H. Hou, W. Dai, Q. Yan, L. Lv, F. E. Alam, M. Yang, Y. Yao, X. Zeng, J.-B. Xu, J. Yu, N. Jiang and C.-T. Lin, *J. Mater. Chem. A*, 2018, **6**, 12091-12097.

16. K. M. Shahil and A. A. Balandin, *Nano Lett.*, 2012, **12**, 861-867.

17. H. Jung, S. Yu, N. S. Bae, S. M. Cho, R. H. Kim, S. H. Cho, I. Hwang, B. Jeong,

J. S. Ryu, J. Hwang, S. M. Hong, C. M. Koo and C. Park, *ACS Appl. Mater. Interfaces*, 2015, **7**, 15256-15262.

18.   P. Min, J. Liu, X. Li, F. An, P. Liu, Y. Shen, N. Koratkar and Z.-Z. Yu, *Adv. Funct. Mater.*, 2018, **28**, 1805365.

19.   X. Shen, Z. Wang, Y. Wu, X. Liu, Y. B. He and J. K. Kim, *Nano Lett.*, 2016, **16**, 3585-3593.

20.   G. Lian, C.-C. Tuan, L. Li, S. Jiao, Q. Wang, K.-S. Moon, D. Cui and C.-P. Wong, *Chem. Mater.*, 2016, **28**, 6096-6104.

21.   Z. Wu, C. Xu, C. Ma, Z. Liu, H. M. Cheng and W. Ren, *Adv. Mater.*, 2019, **31**, e1900199.

22.   Z. Barani, A. Mohammadzadeh, A. Geremew, C. Y. Huang, D. Coleman, L. Mangolini, F. Kargar and A. A. Balandin, *Adv. Funct. Mater.*, 2019, **30**, 1904008.

23.   F. An, X. Li, P. Min, P. Liu, Z. G. Jiang and Z. Z. Yu, *ACS Appl. Mater. Interfaces*, 2018, **10**, 17383-17392.

24.   X.-H. Li, P. Liu, X. Li, F. An, P. Min, K.-N. Liao and Z.-Z. Yu, *Carbon*, 2018, **140**, 624-633.